The Astrophysical Journal, 725:2251–2261, 2010 December 20 doi:10.1088/0004-637X/725/2/2251


# PITCH ANGLE SCATTERING IN THE OUTER HELIOSHEATH AND FORMATION OF THE *INTERSTELLAR BOUNDARY EXPLORER* RIBBON

Konstantin Gamayunov, Ming Zhang, and Hamid Rassoul
Department of Physics and Space Sciences, Florida Institute of Technology, 150 West University Blvd., Melbourne, FL 32901, USA; kgamayunov@fit.edu
*Received 2010 May 12; accepted 2010 October 20; published 2010 December 6*

## ABSTRACT

The dominant and unexpected feature in the first *Interstellar Boundary EXplorer* (*IBEX*) maps is a ribbon of the enhanced energetic neutral atom (ENA) emissions. Presenting the first results from *IBEX*, McComas et al. identified six possible mechanisms of ribbon formation. One of the mechanisms, the so-called secondary ENA mechanism, was already quantitatively elaborated by Heerikhuisen et al., and they successfully reproduced the main features of the ribbon. We further study the "secondary ENA" mechanism by quantifying a previously omitted stage of the proton evolution between two consecutive acts of the charge-exchange in the outer heliosheath (OHS). The main findings can be summarized as follows. (1) The neutrals supplied by the supersonic near-equatorial solar wind dominate the near-equatorial source of the keV ENAs in the OHS compared to the inner heliosheath contribution. (2) The ribbon of the observed width can be produced even if only the large-scale ($\sim 10^2$–$10^4$ AU) interstellar turbulence operates but the resulting pitch angle distribution functions (PADFs) are unstable with respect to the ion cyclotron wave generation around the locus where the line of sight from *IBEX* to the ribbon is perpendicular to the interstellar magnetic field beyond the heliopause. (3) A combination of the large-scale interstellar turbulence and a small-scale ($\sim 10^{-5}$ to $10^{-4}$ AU) turbulence generated by an unstable PADF of the energetic protons is able to make PADF marginally stable. In this case, the ribbon is still narrow because only a small part of the proton phase space distribution function can resonate with a locally generated ion cyclotron turbulence. (4) A concurrent operation of the large-scale interstellar turbulence and the locally generated small-scale turbulence might be responsible for the localized emission structures observed in the *IBEX* ribbon.

*Key words:* ISM: kinematics and dynamics – ISM: magnetic fields – scattering – solar wind – turbulence

## 1. INTRODUCTION

The objective of NASA's *Interstellar Boundary EXplorer* (*IBEX*) mission is to obtain a global view of the interaction between the Sun's solar wind (SW) and the local interstellar medium (LISM). This is accomplished by imaging energetic neutral atoms (ENAs) propagating to Earth from the outer heliosphere (McComas et al. 2009b). *IBEX* was launched into a highly elliptical ($\sim$15,000 km $\times$ 300,000 km) $\sim$8 day orbit on 2008 October 19. The mission payload consists of two single-pixel $7^\circ \times 7^\circ$ sensors: IBEX-Lo measures ENAs from 0.01 to 2 keV (Fuselier et al. 2009a) and IBEX-Hi measures ENAs from 0.3 to 6 keV (Funsten et al. 2009a). These sensors measure ENAs arising from the charge-exchange of both the slower SW protons ($\lesssim$1 keV) and the more energetic pickup ions (PUIs; up to a few keV).

*IBEX* built up its first all-sky energy-resolved maps of ENAs over the first half of 2009 (McComas et al. 2009a; Schwadron et al. 2009; Fuselier et al. 2009b; Funsten et al. 2009b). The dominant feature in all maps is a ribbon of enhanced emissions that extends over a broad range of the ecliptic latitudes and longitudes. The ENA fluxes vary over the ribbon, including a fine structure, with maxima 2–3 times brighter than those from a surrounding region of a more diffuse, globally distributed heliospheric flux (McComas et al. 2009a; Fuselier et al. 2009b). The ribbon is narrow in width (from $\sim 15^\circ$–$25^\circ$) but long, extending over 300° (Fuselier et al. 2009b), and nearly closing a loop in the sky (Funsten et al. 2009b). The ribbon is observed in the energy range from 0.2 keV up to 6 keV with a highest relative intensity at $\sim$1 keV (Fuselier et al. 2009b). In the region of low ecliptic latitudes, a power-law spectral index inside the ribbon slightly exceeds the spectral index in a globally distributed flux (Funsten et al. 2009b). However, the global distribution of the spectral index is predominantly ordered by the ecliptic latitude, regardless of whether it is estimated inside the ribbon or in the globally distributed surrounding flux (Funsten et al. 2009b). This latitudinal dependence is likely due to a latitudinal dependence of the SW velocity, suggesting that transition from the low-latitude slow SW to the high-latitude fast SW controls heating and/or acceleration of the parent ions responsible for ENAs in both the ribbon and the globally distributed surrounding flux.

The *IBEX* ribbon of the ENA emissions was unexpected because this feature was not predicted by any existing model and/or theory of the heliospheric interface (McComas et al. 2009a; Schwadron et al. 2009). So, some new ideas are required to interpret the *IBEX* observations and to advance our understanding of the heliosphere–LISM interaction. Presenting the first results from *IBEX*, Funsten et al. (2009b) pointed out that the ribbon location is likely controlled by the interstellar magnetic field (ISMF) orientation. This, combined with the model results for the heliosphere–LISM interaction, allowed Schwadron et al. (2009) to hypothesize that the ISMF beyond the heliopause (HP) is nearly transverse to the line of sight (LOS) from *IBEX* to the ribbon. In addition, McComas et al. (2009a) identified six possible sources of the enhanced ENA emissions from the ribbon, and one of those ideas has already been quantitatively elaborated by Heerikhuisen et al. (2010). The Heerikhuisen et al. approach to ribbon formation is based on the fact that an average SW ion velocity inside of the termination shock (TS) and in the inner heliosheath (IHS) is anti-sunward. So, after charge-exchange between the SW/IHS protons and the cold interstellar neutrals, a majority of the primary ENAs propagates away from the Sun and a portion of them can reach the outer heliosheath (OHS). The ENAs in the OHS experience charge-exchange again creating energetic protons (the first act of the charge-exchange in OHS). These protons advect along an inhomogeneous ISMF.

They also experience wave-induced pitch angle scattering and loss due to the charge-exchange with a cold and relatively dense interstellar H (the second act of the charge-exchange in OHS). So, the secondary ENAs may be produced by the energetic protons in OHS after the proton evolution during characteristic loss time (see Section 2.1). Then, the sunward propagating ENAs can be detected by *IBEX*. Following Heerikhuisen et al. (2010), we call this mechanism of ribbon formation as a "secondary ENA" mechanism.

Heerikhuisen et al. (2010) simulated formation and transport of the primary ENAs from the inner SW (inside of TS) and IHS into the OHS, the proton production from ENAs, creation of the secondary ENAs from those protons, and finally transport of the secondary ENAs from the OHS to *IBEX*. They successfully reproduced the main features of the *IBEX* ribbon. However, they did not simulate the dynamics and scattering of the OHS protons between two consecutive acts of the charge-exchange. Instead, they introduced a concept of the "partial shell" to crudely approximate the outcome of the scattering process in the OHS that occurs between the moment of the PUI creation and the moment of its re-neutralization. (This concept implies an instantaneous proton scattering over the "partial shell" restricted by the pick up angle and its mirror pair with respect to the 90° angle, but assumes that a secondary ENA production timescale is much shorter than both the advection and the total pitch angle isotropization timescales.) So, the detailed consideration of the energetic proton evolution is required to advance/disadvance the "secondary ENA" mechanism of ribbon formation.

In the present study, we continue the work initiated by Heerikhuisen et al. (2010) by further elaborating a "secondary ENA" mechanism of the ribbon formation. We quantify a previously omitted stage of the energetic proton evolution between two consecutive acts of the charge-exchange in the OHS. This is accomplished by solving the gyro-averaged kinetic equation for the proton phase space distribution function (PSDF). This equation includes proton advection along an inhomogeneous ISMF, the pitch angle focusing/defocusing, the wave-induced pitch angle scattering, and the proton source/loss due to the charge-exchange with cold and dense interstellar $H^+$ and H.

This paper is organized as follows. In Section 2, a set of the governing equations is given along with the ISMF model used in the simulations. We also estimate contributions of the SW and IHS neutrals to a source term in the kinetic equation. In Section 3, we analyze the ribbon formation and stability of the pitch angle distribution function (PADF) with respect to the fast magnetosonic and Alfvén wave generation due to the proton temperature anisotropy. We consider three cases: the case of no pitch angle diffusion, the case of pitch angle diffusion due to the large-scale interstellar turbulence only, and the case of pitch angle diffusion due to a combination of the large-scale interstellar turbulence and a small-scale turbulence self-generated by an unstable PADF of the energetic protons. Also in Section 3, we estimate a relative contribution of the IHS ENAs to ribbon emission. In Section 4, we discuss the results of the ring-beam one-dimensional hybrid simulation and solutions of the wave dispersion equation in the context of the present study. Finally, in Section 5 we provide a summary.

## 2. MODEL

### 2.1. Governing Equations

We assume that the ribbon of ENA emission originates in the LISM outside of the HP due to the charge-exchange of the energetic (∼keV) protons with relatively cold and dense interstellar H. The energetic protons in the OHS are initially supplied by the SW and/or IHS in the form of hydrogen, which is produced by the charge-exchange between the SW/IHS protons and the cold interstellar neutrals in the heliosphere. The energetic H is then charge-exchanged with the cold LISM protons resulting in an energetic proton population there. To model energetic protons, we use the well-known gyro-averaged kinetic equation for the PSDF $f(\mathbf{x}, \mathbf{p}, t)$ (e.g., le Roux et al. 2007). Neglecting the LISM flow speed (26 km s$^{-1}$) compared to the proton speed (430 km s$^{-1}$ for the 1 keV proton), we can write down the resulting equation in the form

$$\frac{\partial f}{\partial t} + v\mu b_i \frac{\partial f}{\partial x_i} + \frac{(1-\mu^2)}{2} v \frac{\partial b_i}{\partial x_i} \frac{\partial f}{\partial \mu} = \frac{\partial}{\partial \mu}\left(D_{\mu\mu}\frac{\partial f}{\partial \mu}\right) + P - L, \quad (1)$$

where $v$, $\mu$, and $\mathbf{b}$ are the velocity, the pitch angle cosine, and the unit magnetic field vector, respectively. The number of protons in the phase space element is given by the equation $dn\ (\mathbf{x}, \mathbf{p}, t) = f(\mathbf{x}, \mathbf{p}, t) 2\pi p^2 dp d\mu$. The three terms in the right-hand side of Equation (1) describe the wave-induced pitch angle scattering with the diffusion coefficient $D_{\mu\mu}$ and the proton production ($P$) and loss ($L$) due to the charge-exchange. Equation (1) is written in a mixed coordinate frame (e.g., le Roux et al. 2007). In this frame, the spatial coordinate $\mathbf{x}$ is measured in the solar frame, while momentum $\mathbf{p}$ is measured in the frame co-moving with the LISM bulk flow. In this study, however, we consider the keV energies only. So, we neglect the difference between the solar and the mixed frames assuming that the Equation (1) solution is close to the solution in the solar frame.

The production and loss terms in Equation (1) have the following forms (e.g., Heerikhuisen et al. 2008):

$$P(\mathbf{x}, \mathbf{p}, t) = f_{\rm H}(\mathbf{x}, \mathbf{p}, t)\, \sigma_{\rm ex}(v)\, v n_{p,\rm LISM}, \quad (2)$$

$$L(\mathbf{x}, \mathbf{p}, t) = f(\mathbf{x}, \mathbf{p}, t)\, \sigma_{\rm ex}(v)\, v n_{\rm H,LISM}, \quad (3)$$

where $f_{\rm H}$ is the PSDF of the energetic H in the LISM, $\sigma_{\rm ex}$ is the H–p charge-exchange cross section, $n_{p,\rm LISM}$ is the cold interstellar proton density, and $n_{\rm H,LISM}$ is the density of the cold H in the LISM. The H–p charge-exchange cross section is taken according to the report by Barnett (1990), and $\sigma_{\rm ex} \approx 2 \times 10^{-15}$ cm$^2$ for the proton energy about 1 keV. For both densities in Equations (2) and (3), we adopt the values used in the simulation by Heerikhuisen et al. (2008), i.e., $n_{p,\rm LISM} = 5 \times 10^{-2}$ cm$^{-3}$ and $n_{\rm H,LISM} = 1.5 \times 10^{-1}$ cm$^{-3}$. The characteristic timescales for the energetic proton production, $T_P = (\sigma_{\rm ex} v n_{p,\rm LISM})^{-1}$, and for the loss, $T_L = (\sigma_{\rm ex} v n_{\rm H,LISM})^{-1}$, are about $T_P \approx 2.7 \times 10^8$ s ≈ 8.6 years and $T_L \approx 9.0 \times 10^7$ s ≈ 2.9 years, respectively. The mean free path (the mean path without charge-exchange) for the neutral population beyond the HP is $L_{\rm H} = (\sigma_{\rm ex} n_{p,\rm LISM})^{-1} \approx 780$ AU. It is likely, however, that the neutral density decreases over that spatial scale as $\sim 1/r^2$.

The widely used quasi-linear approximation for the pitch angle diffusion coefficient is used in the present study. We do not simulate the wave power spectral density self-consistently but rather prescribe it. Observations of the fluctuating SW magnetic fields (e.g., Bieber et al. 1996) show that the fluctuation energy is made up of about 85% of the two-dimensional component (the wave vector is perpendicular to the mean magnetic field) and about 15% of the slab component (the wave vector is parallel/antiparallel to the mean magnetic field). Since

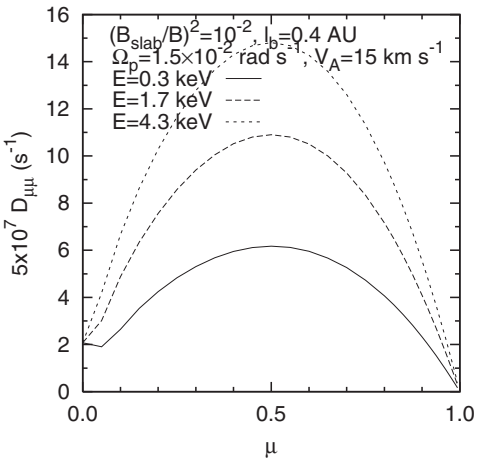


**Figure 1.** Pitch angle diffusion coefficients for the 0.3 keV, 1.7 keV, and 4.3 keV protons vs. pitch angle. The magnetic field is taken to be 1.6 $\mu$G, $n_{p,\mathrm{LISM}} = 5 \times 10^{-2}$ cm$^{-3}$, $(B_{\mathrm{slab}}/B)^2 = 10^{-2}$, and $l_b = 0.4$ AU.

a two-dimensional turbulence component is less effective in the pitch angle scattering than the slab component (Shalchi & Schlickeiser 2004), only a slab component is taken into account in this study. The pitch angle diffusion coefficient is given, for example, by Schlickeiser (1989) for the case of the gyroresonant scattering of the energetic particles by the field-aligned propagating Alfvén and fast magnetosonic waves. For the prescribed non-dissipative Kolmogorov magnetic power spectrum $B^2(k) \approx 2B^2_{\mathrm{slab}} k^{2/3}_{\mathrm{min}}/5/(k^{5/3}_{\mathrm{min}} + k^{5/3})$, and assuming that the forward- and backward-propagating waves have the same intensity, we can write down the diffusion coefficient as

$$D_{\mu\mu} = \frac{\pi}{16}\left(\frac{B_{\mathrm{slab}}}{B}\right)^2 \Omega_p^2 l_b (1-\mu^2)\left[\left(1-\frac{\mu V_A}{v}\right)^2 \times \frac{|\mu v - V_A|^{2/3}}{|\mu v - V_A|^{5/3} + (\Omega_p l_b)^{5/3}} + \left(1+\frac{\mu V_A}{v}\right)^2 \frac{|\mu v + V_A|^{2/3}}{|\mu v + V_A|^{5/3} + (\Omega_p l_b)^{5/3}}\right], \quad (4)$$

where $(B_{\mathrm{slab}}/B)^2$ is the ratio of the slab component magnetic field energy to the background magnetic field energy, $\Omega_p$ is the proton gyrofrequency, $V_A$ is the Alfvén speed, and $l_b = 1/k_{\mathrm{min}}$ is the break wavelength separating the energy range in the wave power spectrum from an inertial range.

For illustration purposes, we show in Figure 1 the diffusion coefficients (4) evaluated for the 0.3 keV, 1.7 keV, and 4.3 keV protons, where ISMF is taken to be 1.6 $\mu$G, $(B_{\mathrm{slab}}/B)^2 = 10^{-2}$, and $l_b = 0.4$ AU.

### 2.2. Interstellar Magnetic Field Model

To specify the magnetic field beyond the HP, we employ a simplified magnetic field configuration resulting from the interaction of the SW and the large-scale ISMF in an extreme case when both the interstellar gas pressure and the dynamic pressure are insignificant compared to the ISMF pressure. This limit was considered by Parker (1961) and, in the first approximation, the resulting magnetic field is given by a superposition of the dipole field and the constant ISMF oriented antiparallel to the magnetic dipole moment. In heliocentric spherical coordinates, with the polar angle ($\theta$) measured from the ISMF direction, the magnetic field outside of the HP ($r > r_{\mathrm{HP}}$) has the following form (Parker 1961):

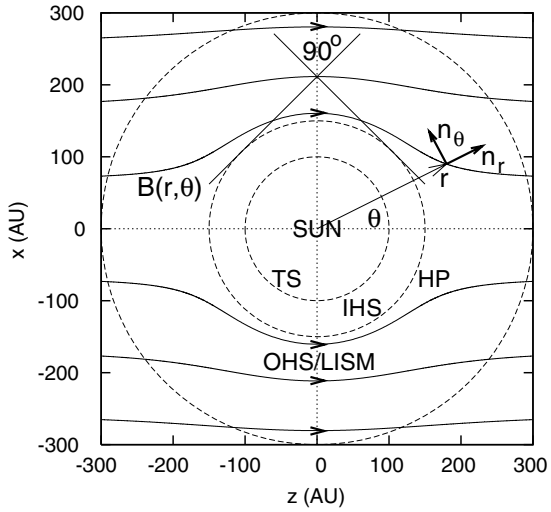


**Figure 2.** Meridional cut of the ISMF used in the simulations. The three concentric circles depict the TS ($r_{\mathrm{TS}} = 100$ AU), the HP ($r_{\mathrm{HP}} = 150$ AU), and the outer boundary of the simulation domain; an entire simulation domain is 150 AU $< r <$ 300 AU. The 90° cone (its apex is placed at $r = 212$ AU) shows that the ENA emission isotropically emitted from the IHS can only be seen inside of the solid angle 360° × 45° by an observer located on the $r = 212$ AU sphere.

$$\mathbf{B}(r,\theta) = B_{\mathrm{LISM}}\left[\mathbf{n}_r \cos\theta\left(1-\left(\frac{r_{\mathrm{HP}}}{r}\right)^3\right) - \mathbf{n}_\theta \sin\theta\left(1+0.5\left(\frac{r_{\mathrm{HP}}}{r}\right)^3\right)\right], \quad (5)$$

where $\mathbf{n}_r$ and $\mathbf{n}_\theta$ are the unit vectors along the $r$- and $\theta$-direction, respectively (see Figure 2), $r_{\mathrm{HP}}$ is the radius of the HP, and $B_{\mathrm{LISM}}$ is the ISMF at the large enough distance from the HP; in all the simulations presented below, we adopt $B_{\mathrm{LISM}} = 4.5\,\mu$G (Opher et al. 2009; Pogorelov et al. 2009) and $r_{\mathrm{HP}} = 150$ AU (Schwadron et al. 2009).

Figure 2 shows schematic of the ISMF as follows from Equation (5). Note that the HP in our simulation does not coincide with the limiting magnetic field lines as expected from the Parker (1961) consideration. We simply assume a spherical HP with a radius of $r_{\mathrm{HP}}$. This is a quite reasonable assumption because (1) the region of the interest in this study is the region around the 90° polar angle where the HP shape is close to a sphere, and (2) the *IBEX* observations suggest that both the ISMF pressure and the LISM dynamic/kinetic pressure are important in shaping the outer heliosphere (McComas et al. 2009a), and so a real magnetic field configuration in the LISM is likely to be something in between the two extremes described by Parker (1961). The TS in our simulations is placed at $r_{\mathrm{TS}} = 100$ AU (Schwadron et al. 2009), and the inner and outer boundaries of the simulation domain are placed at 150 AU and 300 AU, respectively. The 90° cone, with its apex located at $r \approx 212$ AU, shows that the ENA emission isotropically emitted from the IHS can only be seen inside the solid angle 360° × 45° if observed from the $r = 212$ AU sphere; this fact will be used in Section 2.3.

For the magnetic field (5), it is natural to rewrite Equation (1) in heliocentric spherical coordinates as well. It yields

$$\frac{\partial f}{\partial t} + v\mu\left(b_r\frac{\partial f}{\partial r} + \frac{b_\theta}{r}\frac{\partial f}{\partial \theta}\right) + \frac{(1-\mu^2)}{2}v \times \left(\frac{1}{r^2}\frac{\partial r^2 b_r}{\partial r} + \frac{1}{r\sin\theta}\frac{\partial \sin\theta b_\theta}{\partial \theta}\right)\frac{\partial f}{\partial \mu} = \frac{\partial}{\partial \mu}\left(D_{\mu\mu}\frac{\partial f}{\partial \mu}\right) + P - L, \quad (6)$$

where we introduced the unit magnetic field vector as $\mathbf{b} = \mathbf{n}_r b_r + \mathbf{n}_\theta b_\theta$. To solve the kinetic equation (6), we use the "time splitting" method (e.g., Yanenko 1971). The advantage of this method is that a multidimensional problem is split into a sequence of the one-dimensional problems. For each time step, we can obtain an approximate solution to a multidimensional problem by consecutively solving the several one-dimensional problems using results from the previous one as an initial condition for each following problem. The order of the solution operators is reversed during the next time step to achieve a second-order accuracy in time. The first-order advective terms are solved by transporting the PSDF along the corresponding left-hand side characteristics of Equation (6). The analytical solutions for the production and loss terms are used at each time step. The pitch angle diffusion term is solved with the Crank–Nicolson scheme (e.g., Potter 1973), which is an implicit scheme with a second-order accuracy in both the pitch angle and time.

### 2.3. Contributions of SW and IHS Neutrals to the Production Term

The PSDF in the production term (2) is made up of ENAs supplied by the inner SW and IHS due to the charge-exchange between the SW/IHS protons and the cold interstellar neutrals in the heliosphere. The flux of ENAs observed at point $\mathbf{x}$ in the direction $\mathbf{n}$ can be found by collecting the correspondingly directed proton fluxes weighted along the LOS. In the solar frame, neglecting the velocity of the cold interstellar neutrals, the resulting flux of ENAs can be written in the form (e.g., Gruntman et al. 2001)

$$j_{\rm ENA}(\mathbf{x}, \mathbf{n}, p) = \int_{r_1}^{r_2} dr j_p(r, \mathbf{n}, p)\,\sigma_{\rm ex}(v)\,n_{\rm H}(r), \quad (7)$$

where integration is extended over an entire contributing region along the LOS, $j_p(r, \mathbf{n}, p)$ is the flux of the SW or IHS protons in the solar frame, and $n_{\rm H}$ is the number density of the cold interstellar H in the heliosphere; below we adopt $n_{\rm H}(r) = 0.1\,{\rm cm}^{-3}$ in the region from $\sim$10 AU up to $r_{\rm HP}$. Note that we took survival probability to be 1 in Equation (7) (see, e.g., Gruntman et al. 2001), neglecting any particle extinction on their way from the point of birth to the observation point.

We estimate contributions of the SW and IHS neutrals to the production term (2) at the radial distance $r = 212$ AU (see Figure 2). To do that we assume that (1) both the SW PSDF inside of the TS and the IHS PSDF are isotropic in the SW flow frame. This is a reasonable assumption because the SW is highly turbulent, and that leads to a fast pitch angle isotropization. (2) The IHS PSDF is nearly isotropic in the solar frame because the SW velocity is low downstream of the TS but we are interested in the protons with energies $\sim$keV. (3) A majority of the inner SW PSDF (around the SW flow energy, which is of the order of keV) is highly anisotropic in the solar frame because the SW velocity is high upstream of the TS. So, the proton pitch angles are nearly aligned with the radial direction there, and their distribution is close to the $\delta$ function. Finally, (4) the inner SW PSDF depends on the radial distance as $\sim 1/r^2$, while the IHS PSDF does not depend on $r$. After inserting the inner SW proton flux

$$j_{p,{\rm SW}}(r, \mathbf{n}, p) = j_{p,{\rm SW}}(r_1, \mathbf{n}, p)\left(\frac{r_1}{r}\right)^2 \quad (8)$$

into Equation (7), we get the ENA flux at $r_2$ supplied by the SW inside of the TS

$$j_{\rm ENA,SW}(\mathbf{x}, \mathbf{n}, p) = j_{p,{\rm SW}}(r_1, \mathbf{n}, p)\,\sigma_{\rm ex} n_{\rm H} r_1\left(1 - \frac{r_1}{r_2}\right). \quad (9)$$

Using $r_1 = 10$ AU, $r_2 = r_{\rm TS} = 100$ AU, the SW proton number density $n_p(r_1) = 8\,(r_e/r_1)^2 = 8 \times 10^{-2}\,{\rm cm}^{-3}$ (e.g., le Roux et al. 2007), and integrating Equation (9) over the phase space, we can evaluate the number density of ENAs at $r = 212$ AU supplied by the inner SW as

$$n_{\rm ENA,SW}(\mathbf{x}) = n_p(r_1)\,\sigma_{\rm ex} n_{\rm H} r_1\left(1 - \frac{r_1}{r_2}\right) \times \left(\frac{100}{212}\right)^2 \approx 10^{-3}\,{\rm cm}^{-3}, \quad (10)$$

where the factor $(100/212)^2 \approx 0.22$ takes into account that the ENA density decreases as $\sim 1/r^2$ beyond the TS.

Contribution from the IHS neutrals is estimated more roughly. We simply evaluate the right-hand side in Equation (7) as

$$j_{\rm ENA,IHS}(\mathbf{x}, \mathbf{n}, p) = j_{p,{\rm IHS}}(r_1, \mathbf{n}, p)\,\sigma_{\rm ex} n_{\rm H}(r_2 - r_1), \quad (11)$$

where $r_1 = r_{\rm TS}$ and $r_2 = r_{\rm HP}$. The SW velocity is low downstream of the TS, and it is unlikely that a majority of the SW protons produces ENAs in the keV energy range. (Note that, similar to the SW upstream of the TS, the decelerated SW can produce the lower energy ENAs in the near-equatorial region of the slow SW and, probably, the keV ENAs in the high-latitude region of the fast SW.) So, the proton flux in the right-hand side of Equation (11) is actually a flux of the more energetic PUIs in the IHS, i.e., $j_{p,{\rm IHS}}(r, \mathbf{n}, p) = j_{\rm PUI,IHS}(r, \mathbf{n}, p)$. The PUI number density is about 10%–20% of the SW density (e.g., McComas et al. 2009a) but the SW itself is compressed downstream of the TS. Taking the SW density upstream of the TS as $n_p(r_{\rm TS}) = 8(r_e/r_{\rm TS})^2 = 8 \times 10^{-4}\,{\rm cm}^{-3}$, multiplying it by the compression ratio 4 (e.g., le Roux et al. 2007), and taking 15% of the result, we can estimate the PUI number density in the IHS as $n_{\rm PUI}(r_{\rm TS}) \approx 5 \times 10^{-4}\,{\rm cm}^{-3}$. Then, integrating Equation (11) over the phase space, we can evaluate the number density of ENAs supplied by the IHS as

$$n_{\rm ENA,IHS}(\mathbf{x}) = n_{\rm PUI}(r_{\rm TS})\sigma_{\rm ex} n_{\rm H}(r_{\rm HP} - r_{\rm TS})\frac{\Delta\Omega}{4\pi}, \quad (12)$$

where factor $\Delta\Omega/4\pi = [1 - \cos(\pi/4)]/2 \approx 0.15$ takes into account that PSDF in the IHS is spherically isotropic but only ENAs emitted inside the 90° cone shown in Figure 2 can be seen at $r \approx 212$ AU. Finally, inserting all the required numbers in Equation (12), we get

$$n_{\rm ENA,IHS}(\mathbf{x}) \approx 10^{-5}\,{\rm cm}^{-3}. \quad (13)$$

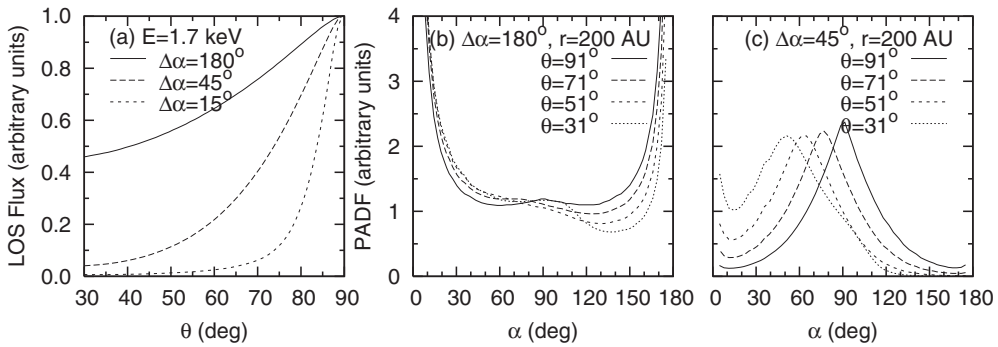


**Figure 3.** (a) Proton fluxes integrated along the radially directed LOS vs. polar angle in the case of $(B_{\rm slab}/B)^2 = 0$ and $E = 1.7$ keV. The source of protons is assumed to be spatially homogeneous, i.e., $F(r) = 1$, and we show results for the source angular widths $\Delta\alpha = 180°$, $\Delta\alpha = 45°$, and $\Delta\alpha = 15°$. (b) PADFs at four polar angles in the case of no pitch angle diffusion, $E = 1.7$ keV, $\Delta\alpha = 180°$, and $r = 200$ AU. (c) Same as (b), except for $\Delta\alpha = 45°$.

A more accurate evaluation of the right-hand side in Equation (7) should increase the estimate (13) but $n_{\rm ENA,SW}(\mathbf{x}) \gg n_{\rm ENA,IHS}(\mathbf{x})$ even after that. So, a contribution of the IHS neutrals to the production term (2) can be neglected compared to the contribution from SW.

To construct PSDF of the energetic neutrals in the LISM ($f_{\rm H}$ in Equation (2)), we take into account that an angular distribution should be organized by the anti-sunward radial direction. In the present study, we take an angular part of the PSDF in a Gaussian form as $\exp\{-[\alpha - \alpha_0(r,\theta)]^2/(\Delta\alpha)^2\}/\sin\alpha$, where $\alpha$ is the ENA pickup angle (the angle between the propagation direction of the parent H and the mean magnetic field at the moment of the charge-exchange), $\alpha_0(r,\theta)$ is the angle between the anti-sunward radial direction and local mean magnetic field, and $\Delta\alpha$ is the typical width of the distribution. We introduced $\sin\alpha$ in the denominator of the angular distribution in order to have distribution $\delta(\alpha-\alpha_0)/\sin\alpha$ in the limiting case of $\Delta\alpha = 0$. The proton momentum in Equation (1) is treated as a parameter, and we simply assume the $\delta$ function for the momentum part of distribution. So, the constructed ENA distribution takes the form

$$f_{\rm H}(\mathbf{x},\mathbf{p},t) = \frac{1}{N}\frac{n_{\rm ENA,SW}}{2\pi p^2}\delta(p-p_0) \times \frac{\exp\left\{-[\alpha-\alpha_0(r,\theta)]^2/(\Delta\alpha)^2\right\}}{\sin\alpha}F(r), \quad (14)$$

where

$$N = \int_0^\pi d\alpha \exp\{-[\alpha-\alpha_0(r,\theta)]^2/(\Delta\alpha)^2\}$$

is the normalization factor, and the radial dependencies $F(r) = 1$ or $F(r) = (r_{\rm HP}/r)^2$ will be used in the following simulations. Note that, as follows from the above estimates, the angular distribution in Equation (14) has to be narrow enough, namely $\Delta\alpha \ll 45°$.

## 3. RESULTS

### *3.1. Simulations without Pitch Angle Diffusion*

We first show the stationary solutions of Equation (6) in the case of no pitch angle diffusion, i.e., in the case $D_{\mu\mu} = 0$. This allows us to look at the best model capability to produce the ribbon because inclusion of the pitch angle diffusion can only make the ribbon less obvious.

Figure 3 shows results of our simulations of the 1.7 keV protons for the spatially homogeneous source in two cases of wide source distributions with $\Delta\alpha = 180°$ and $\Delta\alpha = 45°$ and in the case of a narrow distribution with $\Delta\alpha = 15°$. The proton fluxes integrated along the radially directed LOS versus polar angle are shown in Figure 3(a), and Figures 3(b) and (c) show the PADFs for $\Delta\alpha = 180°$ and $\Delta\alpha = 45°$, respectively.

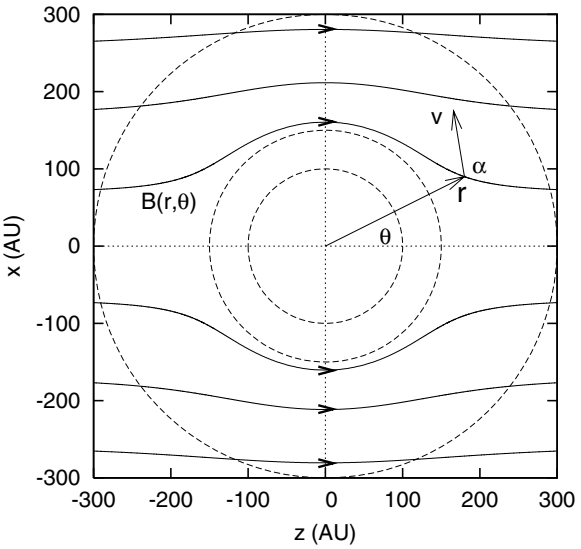


**Figure 4.** Meridional cut of the ISMF along with the radius vector **r** of the proton location, its polar angle $\theta$, velocity **v**, and pitch angle $\alpha$.

It is clearly seen in Figure 3(a) that a moderate enhancement of the ENA emission is produced at $\theta = 90°$ even in the case of a nearly isotropic pith angle distribution of source ($\Delta\alpha = 180°$). The flux of the protons which are moving to $\theta = 90°$ from, for example, the $\theta < 90°$ region increases with $\theta$, and those protons have pitch angles $\alpha > 90°$ (see Figure 4 where both the polar angle and the pitch angle are shown). Therefore, because only the pitch angles $\alpha > 90°$ contribute to the LOS integrated fluxes in the region $0° \leqslant \theta < 90°$, the LOS integrated ENA emissions maximize at $\theta = 90°$ even in the case of the isotropic PSDF of the source. The angle anisotropy of the source becomes important with a decrease of $\Delta\alpha$. The proton source maximizes at the pitch angle $\alpha_0$ but only the PADF "wing" where $\alpha > 90°$ can contribute to the LOS integrated fluxes if $\alpha_0 < 90°$ (or the "wing" $\alpha < 90°$ if $\alpha_0 > 90°$). That is why we see a strong enough ribbon in Figure 3(a) for the case of $\Delta\alpha = 45°$, and especially in the case of $\Delta\alpha = 15°$. Ideally, if there is no pitch angle diffusion, we can produce the ribbon of any strength/width by decreasing $\Delta\alpha$. In the limiting case of $\Delta\alpha = 0$, we get the $\delta(\theta - \pi/2)$ distribution for the LOS integrated flux.

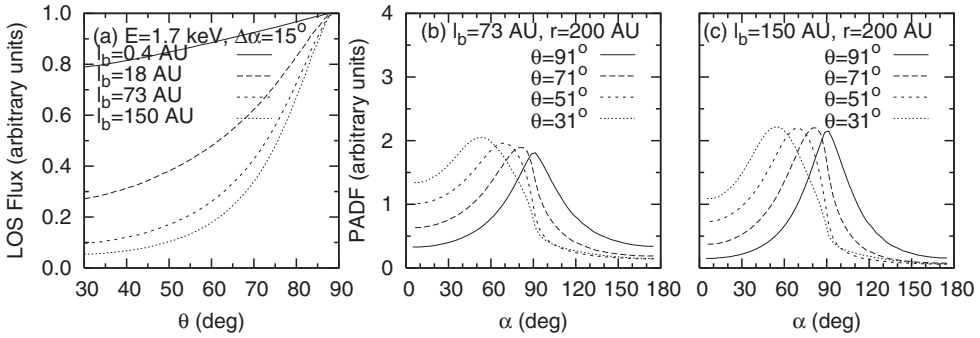


**Figure 5.** (a) Proton fluxes integrated along the radially directed LOS vs. polar angle in the case of $(B_{\rm slab}/B)^2 = 10^{-2}$, $\Delta\alpha = 15^\circ$, and $E = 1.7$ keV. The source of protons is assumed to be spatially homogeneous, and $l_b$ is selected to be 0.4 AU, 18 AU, 73 AU, and 150 AU. (b) PADFs at four polar angles in the case of $(B_{\rm slab}/B)^2 = 10^{-2}$, $\Delta\alpha = 15^\circ$, $E = 1.7$ keV, $l_b = 73$ AU, and $r = 200$ AU. (c) Same as (b), except for $l_b = 150$ AU.

The PADFs in Figures 3(b) and (c) are anisotropic. The low-frequency fast magnetosonic ($\omega = kV_A$) and Alfvén ($\omega = |k_\parallel|V_A$) waves can be unstable in plasma with the anisotropic PADFs. To estimate the stability of the PADFs, we calculate an effective proton temperature along the magnetic field line

$$T_\parallel = \frac{2\pi}{mn_h}\int_0^\infty dpp^4\int_{-1}^1 d\mu\mu^2 f(\mathbf{x},\mathbf{p},t), \qquad (15)$$

and the temperature transverse to the magnetic field

$$T_\perp = \frac{\pi}{mn_h}\int_0^\infty dpp^4\int_{-1}^1 d\mu(1-\mu^2) f(\mathbf{x},\mathbf{p},t), \qquad (16)$$

where $n_h$ and $m$ are the number density of energetic ("hot") protons and their mass, respectively. The parallel temperature in Figure 3(b) exceeds the temperature perpendicular to the magnetic field, and the temperature anisotropy is $A = T_\perp/T_\parallel - 1 \approx -0.3$. For a negative proton anisotropy, the fast magnetosonic waves can be potentially unstable due to the resonant ion cyclotron interaction with protons (e.g., Kennel & Petschek 1966), and Alfvén waves can be unstable due to the firehose instability (e.g., Davidson 1983). The fast magnetosonic waves are unstable if $A < -\omega/(\Omega_p + \omega)$ (Kennel & Petschek 1966), and condition for the firehose instability is $2 + A\beta_\parallel < 0$ (Davidson 1983), where the field-aligned plasma $\beta_\parallel$ for energetic protons is defined as $\beta_\parallel = 8\pi n_h T_\parallel/B^2$. It follows from our simulations that $n_h \approx (2\text{–}3)\times 10^{-4}$ cm$^{-3}$ in the LISM near the HP. Taking 4.5 $\mu$G as an estimate for the ISMF, we get $\beta_\parallel \approx 0.5$ for the 1 keV protons. Therefore, Alfvén waves are likely stable with respect to the firehose instability. The threshold for the fast magnetosonic wave instability in the frequency range $\omega \sim \Omega_p$ can be roughly estimated as $A \lesssim -0.5$. So, the fast magnetosonic waves are also marginally stable/unstable in the case of the PADFs shown in Figure 3(b).

Figure 3(c) shows the PADFs with a large positive anisotropy. The maximum anisotropy is at the polar angle $\theta = 91^\circ$, and is $A \approx 2$. In general, anisotropy maximizes at $\theta = 90^\circ$ decreasing in both directions to the smaller and larger polar angles, and in Figure 3(c) we have $A \approx 0.1$ at $\theta = 31^\circ$. (Note that anisotropy further decreases with decreasing $\theta$, and it is always negative and large enough in the region of the small polar angles where plasma outflows from the system.) In the case of positive anisotropy, Alfvén waves can be unstable due to the resonant ion cyclotron interaction with the energetic protons if $A > \omega/(\Omega_p - \omega)$ (e.g., Kennel & Petschek 1966). In the frequency range $\omega \sim \Omega_p$ (Alfvén waves are usually called ion cyclotron waves in this frequency range), the threshold for instability can be roughly estimated as $A \gtrsim 1$. As a result, Alfvén waves may be unstable in the case of the PADFs shown in Figure 3(c). So, despite the fact that a relatively wide PADF of the source ($\Delta\alpha = 45^\circ$) can produce a strong enough ribbon (see Figure 3(a)), the resulting proton distributions are likely unstable with respect to the ion cyclotron wave generation. Note that anisotropy is much higher in the case of $\Delta\alpha = 15^\circ$ ($A \approx 25$), indicating a strongly unstable PADF in this case.

### 3.2. Simulations with Pitch Angle Diffusion

#### 3.2.1. Large-scale Turbulence

We showed above that PADFs may be unstable, and energetic protons can locally generate a small-scale turbulence resulting in the proton pitch angle scattering. However, the large-scale low-frequency interstellar turbulence (Armstrong et al. 1995) and/or the turbulence resulting from an interaction of the LISM and heliosphere can also scatter protons reducing their anisotropy. Despite the small-scale scattering rate being much greater than the large-scale scattering one, we first consider the effect of turbulence with a large outer scale (large $l_b$ in the pitch angle diffusion coefficient) on the ribbon production and stability of the PADFs. For the *IBEX* energy range ($\leqslant$6 keV), the diffusion coefficient (4) includes the turbulence energy and the break wavelength only in the combination $D_{\mu\mu} \sim B^2_{\rm slab}/B^2/l_b^{2/3}$ if $l_b \gtrsim 10^{-3}$ AU. So, below we hold $(B_{\rm slab}/B)^2 = 10^{-2}$ but change $l_b$ only.

Figure 5 shows results of our simulations in the case of $(B_{\rm slab}/B)^2 = 10^{-2}$, $\Delta\alpha = 15^\circ$, and $E = 1.7$ keV. Similar to Figure 3, the proton source is taken to be spatially homogeneous. We also adopt in Figure 5 the smallest source angular distribution width shown in Figure 3. Figure 5(a) shows the proton fluxes integrated along the radially directed LOS versus polar angle for $l_b = 0.4$ AU, 18 AU, 73 AU, and 150 AU. Figures 5(b) and (c) show the PADFs for $l_b = 73$ AU and $l_b = 150$ AU, respectively. The strong enough ribbons in Figure 5(a) are only seen for $l_b = 73$ AU and 150 AU. In the former case, the anisotropy in Figure 5(b) slightly exceeds +1 at $\theta = 91^\circ$, is about +1 at $\theta \approx 85^\circ$, and $A \approx 10^{-2}$ at $\theta = 31^\circ$. The pitch angle diffusion in the case shown in Figure 5(c) is less strong than in Figure 5(b) resulting in $A \approx 2$ at $\theta = 91^\circ$. The anisotropy decreases to $A \approx 1$ at $\theta \approx 65^\circ$, and we have $A \approx 4\times 10^{-2}$ at $\theta = 31^\circ$. (Note that maximum anisotropies for the cases $l_b = 0.4$ AU and 18 AU shown in Figure 5(a) are $A \approx 0.1$ and $A \approx 0.3$, respectively.) So, if only a large-scale turbulence operates, the source of ENAs with $\Delta\alpha \approx 15^\circ$ can produce the ribbon with a marginally stable PADF in the case of

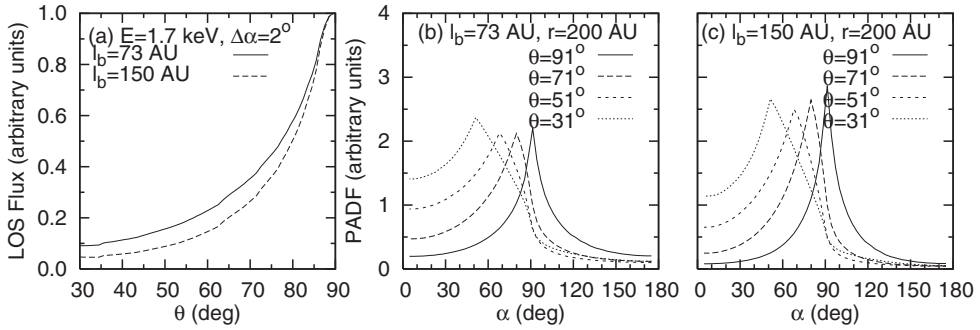


**Figure 6.** (a) Proton fluxes integrated along the radially directed LOS vs. polar angle in the case of $(B_{\rm slab}/B)^2 = 10^{-2}$, $\Delta\alpha = 2^\circ$, and $E = 1.7$ keV. The radial dependence of the proton source is taken in the form of $F(r) = (r_{\rm HP}/r)^2$, and $l_b$ is selected to be 73 AU and 150 AU. (b) PADFs at four polar angles in the case of $(B_{\rm slab}/B)^2 = 10^{-2}$, $\Delta\alpha = 2^\circ$, $E = 1.7$ keV, $l_b = 73$ AU, and $r = 200$ AU. (c) Same as (b), except for $l_b = 150$ AU.

the combination $(B_{\rm slab}/B)^2 \approx 10^{-2}$ and $l_b \approx 70$ AU only. The same conclusion can be made for a larger turbulence level and a larger $l_b$ because $D_{\mu\mu} \sim B_{\rm slab}^2/B^2/l_b^{2/3}$. For example, if we assume $(\delta B)^2 \approx B^2$ and ~15% of the wave turbulence energy in the slab component, then $(B_{\rm slab}/B)^2 \approx 1.5 \times 10^{-1}$, and the turbulence outer scale should be $l_b \approx 4000$ AU in order to keep the PADF marginally stable.

The ribbons in Figure 5(a) are wide enough compared to the *IBEX* observations even in the cases of the large outer turbulence scales $l_b = 73$ AU and 150 AU. It follows from the *IBEX* observations that, on average, the ribbon intensity at $\theta \approx 90^\circ$ is around twice as large as it is at $\theta \approx 80^\circ$ (Schwadron et al. 2009). It is obvious that a narrower angular width of source will result in a narrower ribbon. So, some kind of "realistic" estimate for $\Delta\alpha$ is required. Keeping in mind that we are "working" in the solar frame and $v_{\rm SW} \gg v_{T,\rm SW}$, the source angular width can be roughly estimated as $\Delta\alpha = \arctan(v_{T,\rm SW}/v_{\rm SW})$, where $v_{T,\rm SW}$ is the thermal speed of the SW protons, and $v_{\rm SW}$ is the SW flow velocity. For the SW proton temperature ~1eV observed by the *Voyager 2* spacecraft in the inner heliosphere (Williams et al. 1995), and using $v_{\rm SW} \approx 430\,{\rm km\,s^{-1}}$, we get $\Delta\alpha \approx \arctan(12/430) \approx 2^\circ$. Note that the source distribution will be even narrower in the keV energy range if the SW distribution function is close to the $\kappa$-distribution (Heerikhuisen et al. 2008). On the other hand, the above estimate is given for a proton energy comparable to the SW flow energy, and the source angular distribution should be wider for both the lower and the higher proton energies.

Figure 6 shows results of our simulations in the case of $(B_{\rm slab}/B)^2 = 10^{-2}$, $E = 1.7$ keV, and $\Delta\alpha = 2^\circ$. Compared to Figure 5, the radial dependence of the proton source is now taken in the form of $F(r) = (r_{\rm HP}/r)^2$, and only results for $l_b = 73$ AU and 150 AU are shown. Figure 6(a) shows that the ribbon intensity at $\theta = 90^\circ$ is around twice as large as it is at $\theta = 80^\circ$ for both $l_b = 73$ AU and $l_b = 150$ AU. The pitch angle anisotropy in Figure 6(b) is about +1.5 at $\theta = 91^\circ$, and it decreases to $A \approx 1$ at $\theta \approx 75^\circ$. We have $A \approx -10^{-2}$ at $\theta = 31^\circ$. The anisotropy in Figure 6(c) is much higher than in Figure 6(b), being $A \approx 3$ at $\theta = 91^\circ$, $A \approx 1$ at $\theta \approx 60^\circ$ and $A \approx -2 \times 10^{-2}$ at $\theta = 31^\circ$. So, the ENA source with $\Delta\alpha = 2^\circ$ can potentially produce the desirable ribbon width but the resulting PADFs are unstable with respect to the ion cyclotron wave generation at the polar angles around 90°.

### 3.2.2. Composite Large- and Small-scale Turbulence

The large-scale turbulence cannot keep both the small ribbon width and the PADF stability. For a "realistic" width of the proton source, we can produce the desirable ribbon width but the resulting PADFs are unstable with respect to the ion cyclotron wave generation in the polar angle region around $\theta = 90^\circ$ where $A \gtrsim 1$. The gyroresonance condition for protons and the ion cyclotron waves, $\omega - k_\parallel v_\parallel - \Omega_p = 0$ (e.g., Kennel & Petschek 1966), implies that only protons with the pitch angles $|\mu| \approx V_A(\Omega_p - \omega)/(v\omega)$ can resonate with the waves. The ion cyclotron waves with frequencies closer to $\Omega_p$ become unstable with the anisotropy increase (see Section 3.1), suggesting that the pitch angles of the resonating protons approach $\alpha = 90^\circ$. Although anisotropy maximizes at $\theta = 90^\circ$, below we assume that the pitch angle range,

$$|\mu| \leqslant \frac{V_A}{v}, \tag{17}$$

resonates with the ion cyclotron turbulence in an entire $\theta$-region where $A \gtrsim 1$. In the keV energy range, where $v \gg V_A$, the resonating protons should have pitch angles around 90° if the wave frequencies are not small compared to the proton gyrofrequency. So, Equation (17) is a reasonable assumption for a qualitative analysis of the small-scale turbulence effect. (Note that, in order for any resonance interaction between protons and waves to be strong, the majority of protons should have a parallel velocity comparable to the resonance velocity, i.e., $\left|v_{\parallel,\rm res} - \langle v_\parallel\rangle\right| \lesssim v_{T,\rm SW}$, where $\langle v_\parallel\rangle$ is the average parallel velocity, and $v_{\parallel,\rm res}$ is the resonance velocity. According to Section 2.3, we assumed that the energetic protons in the OHS have a thermal speed comparable to $v_{T,\rm SW}$. For the OHS condition $V_A \approx v_{T,\rm SW} \ll v$ meaning that $\left|\langle v_\parallel\rangle\right| \sim \left|v_{\parallel,\rm res}\right| \lesssim v_{T,\rm SW}$, and the most strong wave–particle interaction takes place for $\alpha_0 \sim 90^\circ$.)

The resonating proton PADF can be made marginally stable in the region $A \gtrsim 1$ by a small-scale self-generated turbulence, while an externally driven large-scale turbulence operates everywhere scattering an entire pitch angle range. In this case, the ribbon will still be narrow because only a small part of the proton PSDF can resonate with the ion cyclotron turbulence according to inequality (17). In this study, we do not simulate the small-scale turbulence self-consistently but rather use the diffusion coefficient (4) obtained for a prescribed Kolmogorov magnetic power spectrum. To model the pitch angle scattering by a small-scale turbulence we specify $l_b = V_A/\Omega_p \approx 10^{-5}$ AU, which is comparable to the field aligned wavelength of the ion cyclotron waves generated in the frequency range $\omega \sim \Omega_p$.

Figure 7 shows both the large- and small-scale turbulence spectra in the case of the non-dissipative Kolmogorov turbulence. The outer scales are set to $l_b = 100$ AU and $l_b = 10^{-5}$ AU for the large- and small-scale turbulence, respectively, and

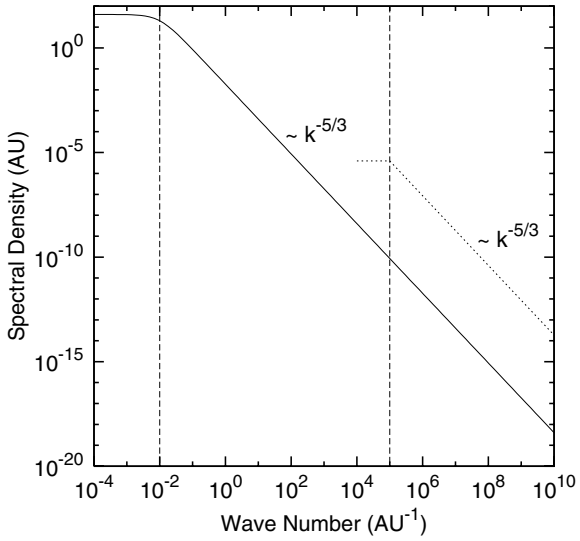


**Figure 7.** Power spectral density for the non-dissipative composite large- and small-scale Kolmogorov turbulence. The outer scales are set to $l_b = 100$ AU and $l_b = 10^{-5}$ AU for the large- and small-scale turbulence, respectively, and shown by the dashed lines. The magnetic energies in both the large- and small-scale turbulence are the same and set to $B^2_{\rm slab} = 1$. The solid line shows the large-scale turbulence spectrum, and the dotted line shows the small-scale one.

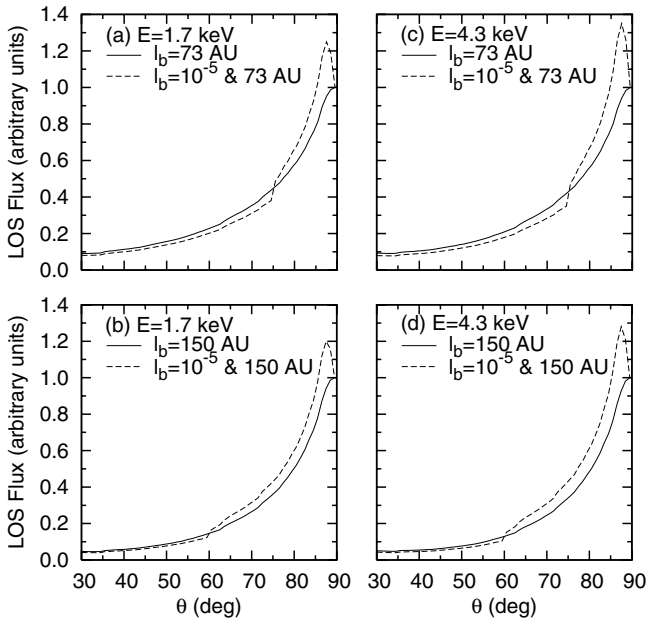


**Figure 8.** (a) Proton fluxes integrated along the radially directed LOS vs. polar angle in the case of $\Delta\alpha = 2^\circ$ and $E = 1.7$ keV. The turbulence level is assumed to be $(B_{\rm slab}/B)^2 = 10^{-2}$ for both large- and small-scale turbulence. The radial dependence of the proton source is taken in the form of $F(r) = (r_{\rm HP}/r)^2$. The solid line shows the case when turbulence with the large outer scale $l_b = 73$ AU is only taken into account. The dashed line is for the case when, in addition to the large-scale turbulence with $l_b = 73$ AU, small-scale turbulence with $l_b = 10^{-5}$ AU is included in the region $75^\circ \leqslant \theta \leqslant 105^\circ$ where only the resonating protons with $|\mu| \leqslant V_A/v$ can interact with the small-scale turbulence. (b) Same as (a), except for $l_b = 150$ AU, and the small-scale turbulence is included in the region $60^\circ \leqslant \theta \leqslant 120^\circ$. (c and d) Same as (a and b), except for $E = 4.3$ keV.

shown by the dashed lines. The magnetic energies in both the large- and small-scale turbulence are the same and simply set to $B^2_{\rm slab} = 1$. The solid line shows the large-scale turbulence spectrum, and the dotted line shows a small-scale one.

We compare in Figure 8 the cases of the large outer scale turbulence only with the cases of composite large- and small-scale turbulence. Figure 8(a) shows the proton fluxes integrated along the radially directed LOS versus the polar angle for $\Delta\alpha = 2^\circ$, and $E = 1.7$ keV. Both the large- and small-scale turbulence levels are set to $(B_{\rm slab}/B)^2 = 10^{-2}$. Similar to Figure 6, the radial dependence of the proton source is taken in the form of $F(r) = (r_{\rm HP}/r)^2$. The solid line shows the case when turbulence with the large outer scale $l_b = 73$ AU is only taken into account. The dashed line is for the case when, in addition to the large-scale turbulence with $l_b = 73$ AU, small-scale turbulence with $l_b = 10^{-5}$ AU is included in the region $75^\circ \leqslant \theta \leqslant 105^\circ$ where only the resonating protons with $|\mu| \leqslant V_A/v$ can interact with the ion cyclotron waves. Figure 8(b) is exactly the same as Figure 8(a), except for $l_b = 150$ AU, and small-scale turbulence is operating in the region $60^\circ \leqslant \theta \leqslant 120^\circ$. Figures 8(c) and (d) show comparisons for $E = 4.3$ keV. It follows from Figures 8(a) and (b) that the inclusion of small-scale turbulence changes the ribbon width only slightly and, similar to Figure 6(a), the difference between the ribbon intensity at maximum and $\theta = 80^\circ$ is about double. Compared to the case of large-scale turbulence only, the composite turbulence displaces the ribbon maximum from $\theta = 90^\circ$ to $\theta \approx 87^\circ$, making an entire ribbon with maximum on both sides of $\theta = 90^\circ$ with a minimum in between. This feature is due to a combination of the large-scale turbulence, which scatters all the pitch angles, and small-scale turbulence operating in the pitch angle region around $90^\circ$ only, but having a diffusion coefficient about $10^4$ times greater compared to the "large-scale" diffusion coefficient. The ribbon has only one maximum if only large or small-scale turbulence operates in an entire pitch angle region. So, a concurrent operation of the large-scale interstellar turbulence and the locally generated small-scale turbulence might be responsible for the localized emission structures observed in the *IBEX* ribbon (McComas et al. 2009a).

As follows from Figures 8(c) and (d), results for $E = 4.3$ keV are very similar to the results in Figures 8(a) and (b). However, we have to note that the $\theta$-region where $A \gtrsim 1$ is wider for the $E = 4.3$ keV case compared to Figures 8(a) and (b) and, probably more important, the source angular distribution is likely to be wider for $E = 4.3$ keV compared to the case of $E = 1.7$ keV.

Figure 8 clearly demonstrates that a composite large- and small-scale turbulence can produce the observed ribbon width and the stable PADF if the turbulence level is set to $(B_{\rm slab}/B)^2 = 10^{-2}$ for both the large- and small-scale turbulence. The turbulence levels in our study were not simulated self-consistently but somewhat arbitrarily prescribed. It is obvious, however, that the ribbon width will increase with $(B_{\rm slab}/B)^2$. So, we are required to look at ribbon widening with increase of the turbulence level. Our knowledge on the outer scale of the large-scale interstellar turbulence is poor, giving us some freedom to change $l_b$. At the same time, it was shown in Section 3.2.1 that for the *IBEX* energy range we can keep the same "large-scale" diffusion coefficient by increasing both $l_b$ and $B_{\rm slab}/B$ because $D_{\mu\mu} \sim B^2_{\rm slab}/B^2/l_b^{2/3}$. In contrast to the large-scale turbulence, we are more or less certain that the outer scale for small-scale turbulence is comparable to the wavelength of the generated ion cyclotron waves. In the present study, we did one more simulation keeping all the parameters as in Figure 8 but the turbulence level was set to $(B_{\rm slab}/B)^2 = 10^{-1}$ on the small scales. The results (not shown) are very close to the corresponding results in Figure 8. This is not surprising because the diffusion coefficient with $l_b = 10^{-5}$ AU and, for example, $(B_{\rm slab}/B)^2 = 10^{-2}$

is about 100 times greater than the maximum diffusion coefficients shown in Figure 1, and it is more than 5000 times greater compared to the case of $l_b = 150$ AU. In the latter case, all the characteristic timescales in Equation (6) are comparable. So, the Equation (6) stationary solution in the case of the composite turbulence should not be sensitive to a "moderate" change of the turbulence level on small scales and/or to the change of the outer scale length for the small-scale turbulence if these changes do not alter the timescale hierarchy. So, the composite large- and small-scale turbulence is able to sustain the observed ribbon width even in the case of the turbulence levels much higher than in Figure 8. In the limiting case, assuming $(\delta B)^2 \approx B^2$ and ~15% of the wave turbulence energy in the slab component for both the large- and small-scale turbulence, we still have the results close to the ribbon shown in Figure 8 but $(B_{\rm slab}/B)^2 \approx 1.5 \times 10^{-1}$.

### 3.3. IHS Contribution to the Ribbon Emission

We can now estimate the relative contribution of the IHS ENAs to the ribbon emission. It follows from our simulation shown in Figure 8(b) that $f\,(r = 153\,{\rm AU})\,2\pi p^2 \Delta p \approx 4 \times 10^{-4}\,{\rm cm}^{-3}$ at $\theta \approx 87^\circ$ for $\alpha \approx 91^\circ$, and $f \sim (r_{\rm HP}/r)^3$ for the polar angles around 90°. To obtain a similar estimate for the IHS, we assume again that the IHS PSDF is isotropic in the solar frame. We maximize an estimate by further assuming that all PUIs have the same energy as in Figure 8(b), i.e., 1.7 keV. Then, we have $f_{\rm IHS} 2\pi p^2 \Delta p = n_{\rm PUI}\,(r_{\rm TS})\,/2$. Using Equation (7) and the results from Section 2.3, a relative contribution of the IHS can be estimated as ($n_{\rm PUI}$ is in the ${\rm cm}^{-3}$ units)

$$\frac{j_{\rm ENA,OHS}}{j_{\rm ENA,IHS}} \approx \frac{4 \times 10^{-4} \times 0.5 r_{\rm HP} n_{\rm H,LISM}}{0.5 n_{\rm PUI}\,(r_{\rm TS})\,(r_{\rm HP} - r_{\rm TS})\,n_{\rm H,IHS}} \approx 3\text{–}5. \quad (18)$$

This estimate is obtained for the polar angles around 90°, and the maximum contribution of the IHS to the ribbon emission from this region is about 20%–33%. So, we have to add $1.2 \times 0.20$–$1.2 \times 0.33 \approx 0.24$–$0.40$ to the dashed line around $\theta = 90^\circ$ in Figure 8(b). The resulting total emissions are 1.44–1.60, 0.84–1.00, and 0.54–0.70 at the polar angles $\theta = 87^\circ$, $\theta = 80^\circ$, and $\theta = 70^\circ$, respectively. In addition, the IHS thickness increases for both the smaller and the larger polar angles, and it is likely that Equation (18) underestimates the IHS contribution. Therefore, an estimate (18), in combination with the results shown in Figure 8, is in a reasonable agreement with the *IBEX* observations, which show that "... ENA fluxes vary over the ribbon, with maxima 2–3 times brighter than the surrounding regions." (McComas et al. 2009a; Fuselier et al. 2009b).

## 4. DISCUSSION

The newly born PUIs in the OHS (after the first act of the charge-exchange in the OHS) have a ring-beam-like PSDF. The ring-beam PSDF is a "richer" one with respect to the low-frequency electromagnetic instabilities than a simple bi-Maxwellian PSDF. However, in this preliminary study we intentionally did not analyze fine structure of the PSDF with respect to fast magnetosonic and ion cyclotron wave instabilities. We rather focused on an analysis of the temperature anisotropy, which is an integral characteristic of the PSDF. This approach, while being rough, allowed us to adopt simple criteria for the low-frequency wave instabilities derived for the case of the bi-Maxwellian energetic proton distribution. We also did not simulate self-consistently the wave magnetic power spectrum but rather used a prescribed Kolmogorov spectrum for the small-scale turbulence assuming that the wave frequencies are not very small compared to the proton gyrofrequency. The validity of our approach could be justified, at least partially, by the results of the hybrid simulation and solutions of the wave dispersion equation in the case of the ring-beam distribution injected in the background plasma.

Recently, Florinski et al. (2010) studied the 1 keV proton evolution in the OHS if an initial ring-beam PSDF is injected in the background LISM. They presented results for protons and electromagnetic field using the one-dimensional (only wave propagation parallel and antiparallel to the external magnetic field is allowed) hybrid simulation. The solid line in Figure 6 from their paper shows the resulting PADF in the case of a broadened ring-beam distribution injected at the angle $\alpha_0 = 85^\circ$ to the ISMF. From this radial direction (where $\alpha_0 = 85^\circ$), only the protons with pitch angle $\alpha = 95^\circ$ can contribute to the LOS flux of the secondary ENAs. From the Florinski et al. Figure 6, we can estimate $f\,(\alpha = 95^\circ) \approx 0.75$. Then, to estimate the ribbon width/intensity we need to know $f\,(\alpha \approx 90^\circ)$ in the case when an initial ring distribution is injected at angle $\alpha_0 \approx 90^\circ$ to the ISMF. Unfortunately, Florinski et al. (2010) did not present results for this case.

Gary & Madland (1988) analyzed the electromagnetic low-frequency instabilities for a specific case of the ring distribution injected at $\alpha_0 = 90^\circ$ to the external magnetic field. They found that a cold ring approximation is only valid for a very small ring temperature in the direction parallel to the external magnetic field. For a ring parallel temperature comparable to the background proton temperature (the thermal proton speed $v_{T,i}$ in their analysis is equal to the Alfvén velocity, similar to the situation in the OHS) the maximum growth rate is more then ten times smaller compared to the cold ring approximation. The temperature of the primary ENAs supplied in OHS (and so the temperature of a newly born PUI ring-beam distribution) is at least not smaller that the SW temperature inside of the TS, which is comparable to the background proton temperature in the OHS. However, Florinski et al. (2010) considered the ring-beam PSDF to be cold in the direction parallel to the ISMF, while they assumed a ring thermal speed $v_{\perp,T} = 225\,{\rm km\,s}^{-1}$ in the perpendicular direction. Using the analytical result from the paper by Wu & Davidson (1972), and parameters from the paper by Florinski et al. (2010), we can estimate the maximum growth rate for the ion cyclotron ring instability in the case of the cold ring distribution injected at angle $\alpha_0 = 90^\circ$ to the ISMF. Then, taking into account that the parallel temperature of the ring distribution is comparable to the background proton temperature, and so reducing the "cold" result by factor of 14 (see Gary & Madland 1988), we get $\gamma/\Omega_p \approx 2 \times 10^{-2}$. According to Figure 2 in the paper by Gary & Madland (1988), the real frequency and wave number of the unstable ion cyclotron mode are $\omega/\Omega_p \approx k V_A/\Omega_p \approx 0.5$. As a result, the equality $\left(\Omega_p - \omega\right)/k v_{T,i} \approx V_A/v_{T,i} \approx 1$ holds for the warm (~1.7eV) background protons in the OHS. This implies that the wave damping rate by the background OHS protons can be estimated as $\gamma_i/\Omega_p \sim -1$ (e.g., Akhiezer et al. 1975). This damping rate overshoots the wave growth making the wave generation impossible. As a consequence, there is no PUI scattering by a self-generated turbulence. In this case, the ring distribution would be stable in the OHS if injected at angles $\alpha_0 \approx 90^\circ$

to the ISMF, and if the pitch angle scattering by the large-scale interstellar turbulence is negligible as claimed by Florinski et al. (2010).

Now, adopting $\Delta\alpha = 2^\circ$ (see Section 3.2.1), and using the dashed line in the Florinski et al. Figure 6, we can estimate $f(\alpha \approx 90^\circ)$ in the OHS in the case when a ring distribution is picked up at $\alpha_0 \approx 90^\circ$ to the ISMF. Simply approximating the PADF by a box with the $4^\circ$ width and centered at $\alpha = 90^\circ$, we get $f(|\mu| \leqslant \cos 88^\circ) \approx (0.5 \times 2.75)/(2 \times \cos 88^\circ) \approx 20$. So, the Florinski et al. (2010) results, combined with the above estimate, suggest that the secondary ENA flux from the radial direction with the $90^\circ$ polar angle is about 27 times higher than flux from the $85^\circ$ radial direction. If we also assume that for the ring-beam injection with $\alpha_0 > 85^\circ$ the resulting PADFs are close to the result shown in the Florinski et al. Figure 6, then the ribbon would be extremely narrow and intense.

The analysis of the ring-beam evolution presented in this section supports the mechanism of the ribbon formation in the OHS. However, the ribbon resulting in this scenario is expected to be extremely narrow and intense compared to the *IBEX* observations. Inclusion in the consideration of the large-scale interstellar turbulence could potentially decrease the ENA flux from the region around polar angle $90^\circ$ but it cannot make the ribbon wider. In this situation the turbulence energy cascade could help. If $B_{\rm slab}/B$ is small, then the parallel wave number cascade is expected to be weak compared to the wave energy cascading in the $k_\perp$ direction (Oughton & Matthaeus. 2005). The possibility of the wave energy cascading was already noted by Florinski et al. (2010). Although, the one-dimensional hybrid simulation by Florinski et al. (2010) precluded the wave energy outflow in the $k_\perp$ direction, they estimated the characteristic energy outflow time as ~500 s for the OHS conditions. This timescale is very small, being actually around the wave period. In this case, a kinetic Alfvén wave ($\omega \sim |k_\parallel| V_A \sqrt{1 + (k_\perp \rho_i)^2}$, where $\rho_i$ is the thermal proton gyroradius) cascade in the $k_\perp$ direction may be an effective channel for the energy transfer to higher frequencies. If this is the case, then the wave energy deficit in the resonant region of the $k$-space would suppress the ring-beam scattering and so make the ribbon wider. It would also bring the situation closer to the scenario outlined in the main body of this study where we assumed for a small-scale turbulence that $\omega \sim \Omega_p$.

## 5. CONCLUSIONS

The dominant feature in the first *IBEX* all-sky maps of the ENAs is a ribbon of enhanced emissions. The ENA emissions vary over the ribbon with maxima 2–3 times brighter than those from a surrounding region of a more diffuse, globally distributed heliospheric flux. The ribbon is narrow in width (~15°–25°) but long, extending over 300° in the sky. The ribbon is observed in the energy range from 0.2 keV up to 6 keV with highest relative intensity at ~1 keV. The *IBEX* ribbon was unexpected because this feature was not predicted by any existing model and/or theory of the heliospheric interface. Presenting the first results from *IBEX*, McComas et al. (2009a) identified six possible mechanisms of the ribbon formation. So far only the "secondary ENA" mechanism of the ribbon formation has been quantitatively elaborated by Heerikhuisen et al. (2010). They successfully reproduced the main features of the *IBEX* ribbon. However, they did not simulate the dynamics and scattering of the OHS PUIs between two consecutive acts of the charge-exchange, but rather introduced a concept of the "partial shell" to crudely approximate the outcome of the scattering process between the time of the PUI creation and its re-neutralization. So, a detailed examination of the energetic proton evolution in the OHS is required to advance/disadvance the "secondary ENA" mechanism of the ribbon formation.

In the present study, we have further elaborated the "secondary ENA" mechanism of ribbon formation. We have quantified a previously omitted stage of the energetic proton evolution between two consecutive acts of the charge-exchange in the OHS. This has been accomplished by solving the gyro-averaged kinetic equation for the proton PSDF. The equation includes the proton advection along an inhomogeneous ISMF, the pitch angle focusing/defocusing, the wave-induced pitch angle scattering, and the proton source and loss due to the charge-exchange with cold and dense interstellar $H^+$ and H. We have analyzed the ribbon formation and stability of the resulting PADF with respect to the low-frequency fast magnetosonic and ion cyclotron wave generation due to the proton temperature anisotropy. Our findings support the "secondary ENA" mechanism of ribbon formation. The main findings are summarized as follows.

1. The near-equatorial source of the keV ENAs in the OHS is more than an order of magnitude dominated by neutrals supplied by the supersonic SW from the near-equatorial slow region compared to the IHS contribution.
2. In the case of no pitch angle diffusion, the ribbon of the observed width can be produced if an angular width of the source PADF is $\Delta\alpha \approx 15^\circ$. However, the resulting temperature anisotropy ($A = T_\perp/T_\parallel - 1$, where $T_\perp$ and $T_\parallel$ are the effective proton temperatures transverse to and along the magnetic field, respectively) is very large ($A \approx 25$) indicating a strongly unstable PADF. The ribbon is extremely narrow and even more unstable for a "realistic" source angular width of $\Delta\alpha \approx 2^\circ$. This suggests that the "secondary ENA" mechanism of the ribbon formation requires, at least, the pitch angle scattering to make the PADF more isotropic and the ribbon wider.
3. In the case of the large-scale interstellar turbulence ($l_b \sim 10^2$–$10^4$ AU, where $l_b$ is the bendover wavelength that separates the energy range in the wave power spectrum from an inertial range), the primary ENA source with $\Delta\alpha \approx 2^\circ$ can produce the observed ribbon width. However, the resulting PADFs are unstable with respect to the ion cyclotron wave generation ($1 \lesssim A \lesssim 3$) around the locus where the LOS from *IBEX* to the ribbon is perpendicular to the ISMF beyond HP. This is true for a wide range of the turbulence level and $l_b$ because the "large-scale" diffusion coefficient scales as $D_{\mu\mu} \sim B_{\rm slab}^2/B^2/l_b^{2/3}$, where $(B_{\rm slab}/B)^2$ is the ratio of the slab component magnetic field energy to the background magnetic field energy. For example, for $l_b \sim 10^2$–$10^4$ AU the turbulence level ranges from $(B_{\rm slab}/B)^2 \sim 10^{-2}$ to $(B_{\rm slab}/B)^2 \gtrsim 10^{-1}$.
4. A combination of the large-scale interstellar turbulence and small-scale ($l_b \sim 10^{-5}$ to $10^{-4}$ AU) turbulence generated by an unstable PADF of the energetic protons is able to make PADF marginally stable in the region around the locus where the LOS is perpendicular to the ISMF. In this case, the ribbon is still narrow because only a small part of the proton PSDF can resonate with locally generated turbulence. If $(B_{\rm slab}/B)^2 = 10^{-2}$ for both the large- and small-scale turbulence, the "small-scale" diffusion time is about $10^3$ times smaller than the "large-scale" diffusion time, which

in turn is comparable to the other characteristic timescales in the kinetic equation. So, the stationary solution is insensitive to the arbitrary increase of the turbulence level on small scales, and to decrease of this level as long as it does not alter the timescale hierarchy in the kinetic equation.

5. A concurrent PUI scattering by the large-scale interstellar turbulence and by the locally generated small-scale turbulence might be responsible for the localized emission structures observed in the *IBEX* ribbon.

Concluding, we would like to emphasize that in this preliminary study we have used a simplified model for the heliosphere–LISM interaction in combination with a semi-quantitative/semi-qualitative analysis. So, while our findings support the "secondary ENA" mechanism of the ribbon formation, a more sophisticated global model of the heliospheric interface should be employed in order to perform a comprehensive stability analysis of an entire PSDF in the OHS. Such a study is a necessary step on the way to further understanding ribbon formation and to advancing our knowledge of interaction between the heliosphere and the galactic medium.

This work was supported in part by NASA under grants NNX09AG29G and NNX09AB24G.

## REFERENCES

Akhiezer, A. I., Akhiezer, I. A., Polovin, R. V., Sitenko, A. G., & Stepanov, K. N. 1975, Plasma Electrodynamics, Vol. 1 (Tarrytown, NY: Pergamon)
Armstrong, J. W., Rickett, B. J., & Spangler, S. R. 1995, ApJ, 443, 209
Barnett, C. F. 1990, Atomic Data for Fusion, Vol. 1, Collisions of H, $H_2$ He and Li Atoms and Ions with Atoms and Molecules, Tech. Rep. ORNL–6086/VI (Oak Ridge, TN: Oak Ridge National Laboratory)
Bieber, J. W., Wanner, W., & Matthaeus, W. H. 1996, J. Geophys. Res., 101, 2511
Davidson, R. C. 1983, in Basic Plasma Phys., Vol. 1, ed. A. A. Galeev & R. N. Sudan (Amsterdam: North-Holland), 519
Florinski, V., Zank, G. P., Heerikhuisen, J., Hu, Q., & Khazanov, I. 2010, ApJ, 719, 1097
Funsten, H. O., et al. 2009a, Space Sci. Rev., 146, 75
Funsten, H. O., et al. 2009b, Science, 326, 964
Fuselier, S. A., et al. 2009a, Space Sci. Rev., 146, 117
Fuselier, S. A., et al. 2009b, Science, 326, 962
Gary, S. P., & Madland, C. D. 1988, J. Geophys. Res., 93, 235
Gruntman, M., Roelof, E. C., Mitchell, D. G., Fahr, H. J., Funsten, H. O., & McComas, D. J. 2001, J. Geophys. Res., 106, 15767
Heerikhuisen, J., Pogorelov, N. V., Florinski, V., Zank, G. P., & le Roux, J. A. 2008, ApJ, 682, 679
Heerikhuisen, J., et al. 2010, ApJ, 708, L126
Kennel, C. F., & Petschek, H. E. 1966, J. Geophys. Res., 71, 1
le Roux, J. A., Webb, G. M., Florinski, V., & Zank, G. P. 2007, ApJ, 662, 350
McComas, D. J., et al. 2009a, Science, 326, 959
McComas, D. J., et al. 2009b, Space Sci. Rev., 146, 11
Opher, M., Alouani Bibi, F., Toth, G., Richardson, J. D., Izmodenov, V. V., & Gombosi, T. I. 2009, Nature, 462, 1036
Oughton, S., & Matthaeus, W. H. 2005, Nonlinear Process. Geophys., 12, 299
Parker, E. N. 1961, ApJ, 134, 20
Pogorelov, N. V., Heerikhausen, J., Mitchell, J. J., Cairns, I. H., & Zank, G. P. 2009, ApJ, 695, L31
Potter, D. 1973, Comput. Phys. (New York: Wiley)
Schlickeiser, R. 1989, ApJ, 336, 243
Schwadron, N. A., et al. 2009, Science, 326, 966
Shalchi, A., & Schlickeiser, R. 2004, ApJ, 604, 861
Williams, L. L., Zank, G. P., & Matthaeus, W. H. 1995, J. Geophys. Res., 100, 17059
Wu, C. S., & Davidson, R. C. 1972, J. Geophys. Res., 77, 5399
Yanenko, N. N. 1971, The Method of Fractional Steps: The Solution of Problems of Mathematical Physics in Several Variables (New York: Springer)